Acta Mechanica Sinica (2014) 30(4):457–467
DOI 10.1007/s10409-014-0068-z

REVIEW

Space-time correlations in turbulent Rayleigh–Bénard convection

Xiaozhou He · Penger Tong

Received: 29 May 2014 / Accepted: 4 June 2014

Abstract The recent development of the elliptic model (He, et al. Phy. Rev. E, 2006), which predicts that the space-time correlation function $C_u(r,\tau)$ in a turbulent flow has a scaling form $C_u(r_E,0)$ with r_E being a combined space-time separation involving spatial separation r and time delay τ, has stimulated considerable experimental efforts aimed at testing the model in various turbulent flows. In this paper, we review some recent experimental investigations of the space-time correlation function in turbulent Rayleigh–Bénard convection. The experiments conducted at different representative locations in the convection cell confirmed the predictions of the elliptic model for the velocity field and passive scalar field, such as local temperature and shadowgraph images. The understanding of the functional form of $C_u(r,\tau)$ has a wide variety of applications in the analysis of experimental and numerical data and in the study of the statistical properties of small-scale turbulence. A few examples are discussed in the review.

Keywords Turbulent Rayleigh–Bénard convection · Elliptic model · Space-time correlations

1 Introduction

Fluid turbulence is characterized by a fluctuating velocity field $\boldsymbol{u}(\boldsymbol{x},t)$ at position $\boldsymbol{x}$ and time t. The statistical properties of $\boldsymbol{u}(\boldsymbol{x},t)$ can be described by the normalized correlation function at two space-time points separated by a spatial distance r and time delay τ,

$$C_u(r,\tau) \equiv \frac{\langle u(x+r,t+\tau)u(x,t)\rangle_t}{\sigma_u(x+r)\sigma_u(x)}, \tag{1}$$

where $\sigma_u(x+r)$ and $\sigma_u(x)$ are, respectively, the root-mean-square (rms) values of the local velocity at positions $x+r$ and x. For simplicity, we only consider a one-dimensional case in Eq. (1), assuming that both the mean flow and its fluctuations are along the x-direction. One can readily extend the definition to three-dimensional flows, in which case the correlation function becomes a tensor field. Understanding the relationship between space and time in the velocity correlation function $C_u(r,\tau)$ (or a passive-scalar correlation function) has long been a fundamental issue in statistical theories of small-scale turbulence and is also a common problem in the general areas of fluid dynamics, non-equilibrium statistical physics, geophysics and astrophysics [1–3].

In theories of turbulence, the equal-time correlation function $C_u(r,0)$ or its Fourier transform $E_u(k)$ is often used to describe the spectrum of turbulent kinetic energy in different lengths r or wave numbers k. For example, Kolmogorov's self-similarity hypothesis [4] predicted that the wave-number energy spectrum $E_u(k)$ of local velocity fluctuations scales as, $E_u(k) \sim k^{-5/3}$, in the inertial subrange. For near-wall turbulence, the velocity wave-number spectrum in the log-layer is predicted to have the form, $E_u(k) \sim k^{-1}$, based on Townsend's attached-eddy hypothesis [5]. Direct measurement of these quantities, however, is still a challenging task for experiment. This is partially due to the fact that such direct measurements require high resolutions both in space and time over a large viewing area and a long measuring period of time. While recent developments of particle image velocimetry (PIV) allow one to obtain more spatial information for small-scale flows, time-domain measurements continue to play a major role in the experimental study of large-scale flows, such as turbulent jets and wind tunnels [6, 7]. From the time series measurement of the local velocity (or a passive scalar) at a single or a few spatial positions, one can obtain the temporal correlation function $C_u(0,\tau)$ or its

X. He (✉)$_1$ · P. Tong (✉)$_2$
Department of Physics,
Hong Kong University of Science and Technology,
Clear Water Bay, Kowloon, Hong Kong, China
e-mail$_1$: xiaozhou.he@ds.mpg.de
e-mail$_2$: penger@ust.hk

X. He
Max Planck Institute for Dynamics and Self Organization,
D-37073 Göttingen, Germany

Fourier transform, the frequency spectrum $E_u(f)$. Finding a relationship between space and time, which connects the time-domain results to the theoretical predictions made in the real space (or in the Fourier ($k-$) space) is, therefore, of fundamental interest and practical importance to the study of fluid turbulence.

In 1938, Taylor first proposed the frozen-flow hypothesis [8] in that the spatial structures of a turbulent flow field can be inferred from the temporal fluctuations at a fixed downstream-wise position by a linear transformation between the spatial separation r and the time delay τ. The coefficient which links the two quantities is the mean flow velocity U_0. Taylor's hypothesis requires a long correlation length and, thus, is valid only for a special group of flows in which the mean flow velocity U_0 is much larger than the velocity fluctuations. It was first tested in a grid-generated turbulent flow in wind tunnel [8]. After that the Taylor frozen-flow hypothesis has been widely used in the analysis of statistical properties of the single-point velocity (and passive scalar) measurements conducted in turbulent wind tunnels and in other flow systems [9, 10].

For isotropic turbulent flows, where there is no mean flow ($U_0 = 0$), the Taylor frozen-flow hypothesis is not expected to be valid. Kraichnan [11] postulated the random sweeping hypothesis in that small-scale fluctuations are passively swept by large eddies in the flow, so that the flow micro-structures are statistically independent of the large eddies. Based on this hypothesis, Tennekes [12] showed that the effect of flow fluctuations on the Eulerian frequency spectrum or temporal structure function is to increase advective broadening. In the inertial subrange, the random sweeping hypothesis leads to that the Eulerian frequency spectrum of local velocity fluctuations has the form $E_u(f) \sim f^{-5/3}$. This scaling form is the same as the wave-number spectrum $E_u(k)$ predicted by Kolmogorov's 1941 self-similarity hypothesis [4, 13]. Consequently, Kraichnan's random sweeping hypothesis yields a linear relation between the wave number k and frequency f, or equivalently between r and τ. The coefficient which links the two quantities is the random sweeping velocity σ_u.

For many practical flows of interest, such as turbulent jets, channel flows and turbulent thermal convection where the mean velocity U_0 is comparable to the rms velocity σ_u, neither Taylor's frozen-flow hypothesis nor Kraichnan's random sweeping hypothesis holds. Attempts have been made to deal with those flows in which the characteristic time associated with small dissipative eddies is finite but not infinite, which is required by Taylor's frozen-flow hypothesis. With the so-called "local Taylor hypothesis" [14], the space variable x is connected to time τ via the equation $x = \int_0^\tau u(0,t)\mathrm{d}t$, where the integral τ is chosen to be less than the largest time associated with the energy containing eddies in the flow. The local Taylor hypothesis was first applied to von Kármán swirling flow [15] and then to turbulent Rayleigh–Bénard convection (RBC) [16–18]. It is applicable only to the time series measurement of local velocities but is not useful for passive scalars [19].

More recently, Zhao and He [20] proposed a model showing that the space-time correlation function $C_u(r,\tau)$ has a scaling form $C_u(r_E, 0)$ for a stationary and homogenous flow with the combined space-time separation r_E being of the elliptic form

$$r_E^2 = (r - U\tau)^2 + V^2\tau^2. \tag{2}$$

Here U is a characteristic convection velocity proportional to the mean flow velocity U_0 and V is associated with a random sweeping velocity proportional to the rms velocity σ_u. This so-called elliptic model incorporates both Taylor's frozen-flow hypothesis when V is small and Kraichnan's random sweeping hypothesis for a homogenous and isotropic turbulent flow with $U \simeq 0$. Zhao and He [20, 21] showed that the scaling form $C_u(r_E, 0)$ is mathematically exact up to the second order of $C_u(r,\tau)$ and numerically demonstrated that it also hold for large values of r and τ because of the scale-invariance of the turbulent flow.

The elliptic model has stimulated considerable experimental efforts aimed at testing it in various turbulent flows. It was first tested in a turbulent RBC experiment using temperature $T(\boldsymbol{x}, t)$ as a passive scalar field [22, 23]. It was then further verified in the velocity field [24] and applied to the shadowgraph image measurements [25] in RBC. More recently, the elliptic model was extended to Lagrangian velocities in isotropic turbulence [26] and was also used in deriving the energy spectrum in the wave-number-frequency space for random sweeping flows with an additional mean speed [27]. In this paper, we review some recent developments in the experimental investigation of space-time correlation functions in turbulent RBC.

2 Elliptic approximation for space-time correlations

In the elliptic model, Zhao and He [20, 21] showed that for a spatially homogeneous and statistically stationary one-dimensional turbulent flow, the first-order terms in the Taylor-series expansion of the correlation function

$$\begin{aligned} C_u(r,\tau) = C_u(0,0) &+ \frac{\partial C_u(0,0)}{\partial r} r \\ &+ \frac{\partial C_u(0,0)}{\partial \tau}\tau + \frac{\partial^2 C_u(0,0)}{\partial r \partial \tau} r\tau \\ &+ \frac{1}{2}\left(\frac{\partial^2 C_u(0,0)}{\partial r^2} r^2 + \frac{\partial^2 C_u(0,0)}{\partial \tau^2}\tau^2\right) + \cdots \end{aligned} \tag{3}$$

vanish. As a result, Eq. (3) can be written as a complete square form

$$C_u(r,\tau) = C_u(0,0) - \frac{1}{2}\frac{r_E^2}{\lambda_0^2} + \cdots, \tag{4}$$

where the combined space-time separation r_E is given by Eq. (2) and $\lambda_0^2 = -(\partial^2 C_u(0,0)/\partial r^2)^{-1}$ is the Taylor micro

scale. In the above, the two characteristic velocities U and V are determined by the second derivatives of $C_u(r,\tau)$ at the origin

$$U = -\frac{\partial^2 C_u(0,0)}{\partial r \partial \tau}\left(\frac{\partial^2 C_u(0,0)}{\partial r^2}\right)^{-1}, \tag{5}$$

and

$$V^2 = \frac{\partial^2 C_u(0,0)}{\partial \tau^2}\left(\frac{\partial^2 C_u(0,0)}{\partial r^2}\right)^{-1} - U^2. \tag{6}$$

Evidently, Eq. (4) is valid only for small values of r and τ, as it is a second-order Taylor expansion. Zhao and He [20, 21] proposed that if a turbulent flow becomes scale-invariant in the inertial range at a sufficiently large Reynolds number, $C_u(r,\tau)$ should have a self-similar form

$$C_u(r,\tau) \simeq C_u(r_E, 0), \tag{7}$$

even for large values of r and τ. Using the direct numerical simulation (DNS) data, Zhao and He [20] verified Eq. (7) in a turbulent channel flow. It was found that the velocity U in Eq. (2) is associated with the mean flow velocity U_0 and V is given by

$$V = [\sigma_u^2 + (S\lambda_0)^2]^{1/2}, \tag{8}$$

where S is the shear rate of the flow. For turbulent convection at the cell center [22] and turbulent pipe flows near the central line, the term $S\lambda_0$ is negligibly small and thus one has $V \simeq \sigma_u$.

Because $C_u(r,\tau)$ is averaged over the space and time, the two characteristic velocities are actually the space-time averaged velocities. When the mean flow velocity U_0 is much larger than its rms value σ_u, the elliptic model as described in Eqs. (2)–(7) leads to the same result as the Taylor hypothesis does. For an isotropic random sweeping flow where the flow fluctuations dominate, the elliptic model gives the same prediction as that made by Kraichnan's random sweeping hypothesis. The elliptic model thus naturally incorporates both Taylor's frozen-flow hypothesis and Kraichnan's random sweeping hypothesis. It is expected to be applicable to a large class of turbulent flows which are characterized by a combination of mean and rms velocities.

Figure 1 shows the iso-correlation contour plots of $C_u(r,\tau)$ [$= C_u(r_E, 0)$] in the r–τ plane for different values of r_E given in Eq. (2) with $U = 14.0$ mm/s and $V = 11.2$ mm/s. It is seen that the iso-correlation contours appear as a set of elliptic curves having the same origin, orientation and aspect ratio. For a given value of r_E, the amplitude of $C_u(r,\tau)$ for different values of r and τ satisfying Eq. (2) remains the same, as indicated in Eq. (7). Therefore, Eq. (2) describes the functional form of the iso-correlation contour of $C_u(r,\tau)$. The aspect ratio and orientation angle of the elliptic contours are determined by the values of U and V [21]. When $U = 0$, the set of elliptic contours has a standard form of the ellipse with its two major axes coincided with the r and τ axes, respectively. Substituting $U = 0$ into Eq. (2), one finds [23]

$$\frac{r^2}{a^2} + \frac{\tau^2}{b^2} = 1, \tag{9}$$

where $a = r_E$ and $b = r_E/V$. When $V = 0$, Eq. (2) becomes

$$r = r_E + U\tau. \tag{10}$$

In this case, the Taylor frozen-flow hypothesis is valid and the iso-correlation contours of $C_u(r,\tau)$ are represented by a set of straight lines with a slope of U and intercept equal to r_E [21].

Because the Taylor expansion and flow similarity assumption are quite general, the elliptic model is also expected to be useful for the study of other space-time functions that are used to describe the statistical properties of small-scale turbulence. Examples of those space-time functions include higher-order space-time correlation functions, space-time structure functions, and space-time joint probability density functions. In this review, we focus our attention on the space-time correlation functions $C_u(r,\tau)$ and $C_T(r,\tau)$.

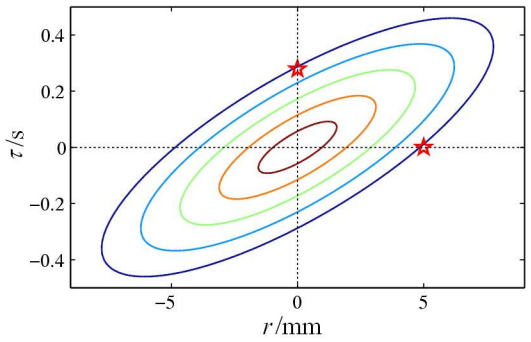

Fig. 1 Iso-correlation contour plots of $C_u(r,\tau)$ [$= C_u(r_E, 0)$] in the r-τ plane for different values of r_E given in Eq. (2) with $U = 14.0$ mm/s and $V = 11.2$ mm/s. The two stars indicate two special positions $(r_0, 0)$ and $(0, \tau_0)$; both of them satisfy Eq. (2) for a common value of r_E

3 Experimental tests of the elliptic model

3.1 Turbulent Rayleigh–Bénard convection

Turbulent RBC is a model system for the study of convective turbulence [19, 28–30]. The convective flow is generated in a confined system between two horizontal plates separated by a distance L and heated from below in the presence of gravity. The flow properties in RBC are determined by three dimensionless parameters: the Rayleigh number $Ra \equiv \alpha g \Delta T L^3/\nu\kappa$, the Prandtl number $Pr \equiv \nu/\kappa$, and the aspect ratio $\Gamma \equiv D/L$ of the convection cell. Here g is the gravitational acceleration, ΔT is the temperature difference between the two horizontal plates of lateral dimension D, and α, ν, and κ are, respectively, the thermal expansion coefficient, the kinematic viscosity, and the thermal diffusivity of the convecting fluid.

When the dimensionless buoyancy force Ra is sufficiently large, the fluid close to the heating and cooling plates becomes unstable and moves into the interior of the fluid.

These active fluid parcels are known as thermal plumes. When the convection reaches a steady state, the thermal plumes in the $\Gamma \simeq 1$ cell organize themselves into a single large-scale convection roll (also known as the large-scale circulation, or LSC), which moves from the bottom to the top and vice versa along the sidewall. Such a convective flow is also associated with an inhomogeneous distribution of turbulent temperature field. It was found [31, 32] that the temperature difference ΔT across the cell is concentrated mainly in two thin thermal boundary layers adjacent to the bottom and top conducting plates. There are only a few percent of ΔT dropped across the bulk region of the convecting fluid. Recent experiments [33] revealed that the mean temperature profile across the bulk fluid varies logarithmically along the vertical direction and is symmetric about the mid-height plane of the cell.

Near the mid height, the logarithmic temperature profile yields a minimum vertical gradient in the mean temperature, which leads to a negligibly small buoyancy compared to the advection by the convective flow. As a result, temperature field around the mid-height of the cell is a passive scalar to a very good approximation, which has been confirmed by previous studies [18, 34]. Only within the thermal boundary layers where the buoyancy reaches the maximum and becomes dominant over the flow advection as the convective flow velocity diminishes because of the non-slip boundaries, the temperature behaves like an active scalar [35, 36].

The velocity field in a $\Gamma = 1$ convection cell with $1 \times 10^9 \lesssim Ra \lesssim 1 \times 10^{10}$ and $Pr \simeq 5$ has been carefully studied previously [37]. In the rotation plane of the LSC, the flow has a fly wheel structure with a zero mean velocity at the cell center and an increasing mean vertical velocity along the horizontal cell diameter at the mid-height. After reaching its maximum value near the sidewall ($\sim 0.05D$ away from the sidewall), the mean vertical velocity starts to drop quickly and becomes zero at the cell wall because of the non-slip boundary condition. Therefore, the velocity field near the sidewall at the mid-height is similar to that of a channel flow with a mean vertical velocity U_0 and a rms velocity $\sigma_v \simeq 0.6U_0$ [37]. In the central region of the cell, on the other hand, the flow is close to a homogeneous and isotropic turbulent flow [38] with the mean velocity $U_0 = 0$. At these two locations, the Taylor frozen-flow hypothesis is not expected to hold.

3.2 Temperature space-time correlations

Similar to Eq. (1), the normalized correlation function of temperature fluctuations at two space-time points separated by a spatial distance r and time delay τ is defined as

$$C_T(r,\tau) = \frac{\langle \delta T(x+r,t+\tau)\delta T(x,t)\rangle_t}{\sigma_T(x+r)\sigma_T(x)}, \tag{11}$$

where $\langle\cdots\rangle_t$ denotes a time average, $\delta T = T - \langle T\rangle_t$, and $\sigma_T(x+r)$ and $\sigma_T(x)$ are, respectively, the rms values of the local temperature fluctuations at positions $x+r$ and x. Because the temperature at the cell mid-height behaves like a passive scalar at the cell center and near the sidewall, the temperature space-time correlation function $C_T(r,\tau)$ at the two locations is expected to have the same form as that of $C_u(r,\tau)$.

In the experiment, $C_T(r,\tau)$ is obtained from the two-point temperature measurement, which are simultaneously taken by two thermistors of diameter 0.2 mm with a spatial separation r. Details about the temperature measurements have been described in Ref. [39]. Near the sidewall, the two thermistors are placed one above another with the vertical separation r varying from 0 to 16 mm along the downstream direction. In the central region, one thermistor is fixed at the cell center and the other (mobile) thermistor is placed at the same height as the fixed one with a horizontal separation r. The value of r is varied from 0.1 to 90 mm. All the temperature measurements are conducted in the plane of the LSC. Great care is taken to align the two thermistors at an accuracy better than 30 μm. Typically, we take 10 h-long time series data at each location with a sampling rate of 40 Hz ($> 10^6$ total data points) in order to ensure adequate statistics.

We first examine the spatial dependence of the single-point temperature statistics near the sidewall. Figure 2a shows the measured probability density function (pdf) $P(\delta T)$ of the normalized temperature fluctuations $\delta T/\sigma_T$ near the sidewall. The measurements are made at different vertical locations above the mid height of the cell. All the pdf curves with varying vertical positions are well superimposed with each other over an amplitude range of approximately 5 decades. Because the convection cell is tilted by a small angle in such a way that the up-going large-scale flow passes through the thermistors, the temperature pdfs are all asymmetric and are skewed toward the positive δT. Figure 2b shows the position dependence of the measured $\langle T(x+r) - T(x)\rangle_t$ (red solid squares), rms value $\sigma_T(x+r)$ (red open squares), and skewness $S_k(x+r)$ (black solid circles) of the local temperature fluctuations at different locations r near the sidewall. These measurements suggest that the single-point temperature statistics near the sidewall, as described by the temperature pdf $P(\delta T)$, local temperature variation $\langle T(x+r) - T(x)\rangle_t$, rms value $\sigma_T(x+r)$ and skewness $S_k(x+r)$, are all homogeneous and independent of the measuring position r up to around 14 mm (vertical dashed line).

Figure 3a shows the measured temporal auto-correlation function $C_T(0,\tau)$ of temperature fluctuations near the sidewall with varying vertical positions r. It is seen that the measured $C_T(0,\tau)$ remains unchanged with the measuring position r. Without any slow drift in the temperature data, all the correlation curves decay to 0 when $|\tau| \simeq 10$ s. Figure 3b shows the magnified plots in Fig. 3a for small values of τ. All the the measured $C_T(0,\tau)$'s are symmetric about $\tau = 0$, as expected for stationary temperature fluctuations. In the range of $|\tau| \leqslant 0.1s$, the measured $C_T(0,\tau)$ can be well described by a parabola function, $C_T(0,\tau) = 1 - (1/2)(\tau/\lambda_\tau)^2$, with λ_τ being a decay time in analogous to Taylor's micro-

scale as defined in Eq. (4) [10]. In the central region of the cell, we obtain similar results as shown in Figs. 2 and 3 (not shown here). Our measurements thus demonstrate that the temperature statistics at the two locations are spatially homogeneous and statistically stationary, as required by the elliptic model.

Figure 4a shows a three-dimensional (3D) plot of the measured space-time correlation function $C_T(r,\tau)$ as a function of r and τ near the sidewall. The amplitude of the measured $C_T(r,\tau)$ decays monotonically along the two directions from the peak value of $C_T(0,0) = 1$ at the origin. The single peaked function of $C_T(r,\tau)$ ensures that the iso-correlation contours are closed curves and that $C_T(r,\tau)$ is differentiable with respect to r and τ. Figure 4b shows a 2D plot of the iso-correlation contours of the measured $C_T(r,\tau)$ in the r–τ plane. From the inner to outer curves, the correlation amplitude is varied from 0.98 to 0.8 with a decrement of 0.02. It is seen that in the r-τ plane explored, all the iso-correlation contours have a similar elliptic shape, as predicted in Eq. (2). They appear as a common set of elliptic curves having the same orientation and aspect ratio, as shown in Fig. 1. The fact that the iso-correlation contours are tilted at an angle with respect to the r-axis suggests that both the values of U and V are nonzero, as shown in Eq. (2).

Figure 5a shows a 3D plot of the measured $C_T(r,\tau)$ as a function of r and τ at the center of the convection cell, where the mean velocity $U_0 = 0$. Similar to the situation near the sidewall, the measured $C_T(r,\tau)$ is a single peaked function with a maximal value of $C_T(0,0) = 1$ at the origin and decays monotonically to zero at large values of r and τ. Figure 5b shows a 2D plot of the iso-correlation contours of the measured $C_T(r,\tau)$ at the cell center with the correlation amplitude varied from 0.95 to 0.4 at decrements of 0.05 (from inner to outer contours). The obtained iso-correlation contours appear as a set of ellipses having the same orientation and aspect ratio. The long and short major axes of the ellipses coincide with the r and τ axes, respectively. The shape of the iso-correlation contours is well described by the standard elliptic function as given in Eq. (9). From Eq. (9), one finds that the ratio of the long axis to the short axis for each ellipse is directly related to the rms velocity V via $a/b = V$. With this relationship, one can obtain V directly from the iso-correlation contours as shown in Fig. 5b [23].

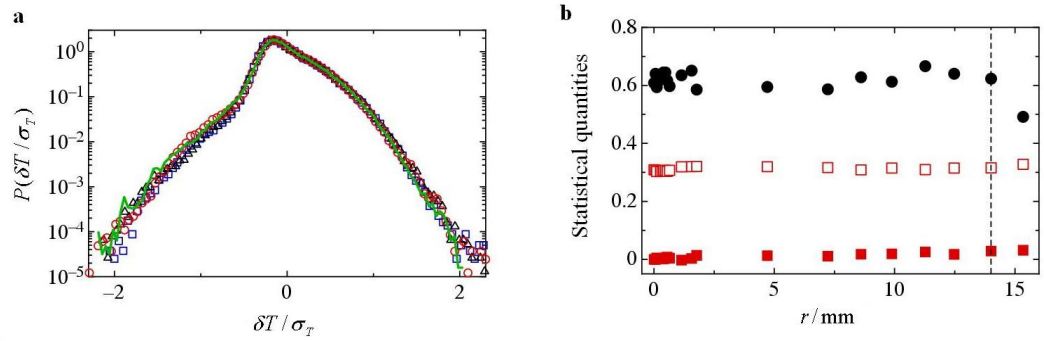

Fig. 2 (Colour online) **a** Measured probability density function $P(\delta T)$ of the normalized temperature fluctuations $\delta T/\sigma_T$ near the sidewall. The measurements are made using the mobile thermistor for different vertical distance above the mid height: $r = 0.98$ mm (blue squares), 2.78 mm (black triangles), 7.22 mm (red circles), and 12.47 mm (green line). All the measured $P(\delta T)$ are normalized so that their integration over $\delta T/\sigma_T$ is 1; **b** Measured $\langle T(x+r)-T(x)\rangle_t$ (red solid squares), rms value $\sigma_T(x+r)$ (red open squares), and skewness $S_k(x+r)$ (black solid circles) of the local temperature fluctuations at different locations r near the sidewall. All the measurements are made at $Ra = 1.4\times10^{10}$

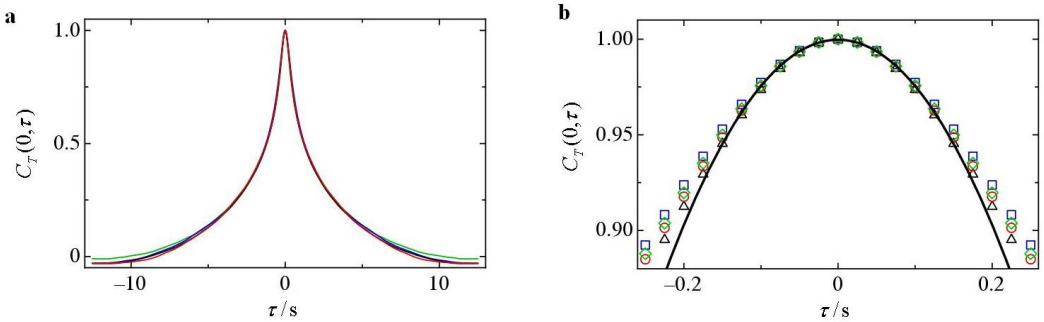

Fig. 3 (Colour online) **a** Measured temporal correlation function $C_T(0,\tau)$ of temperature fluctuations near the sidewall. The measurements are made using the mobile thermistor for different vertical distance above the mid height: $r = 0.98$ mm (blue curve), 2.78 mm (black curve), 7.22 mm (red curve), and 12.47 mm (green curve); **b** Magnified plots in a for small values of τ. The black solid line shows the fitted function $C_T(0,\tau) = 1 - (1/2)(\tau/\tau_0)^2$ to the diamonds with $|\tau| \leqslant 0.1$ s. All the measurements are made at $Ra = 1.4\times10^{10}$

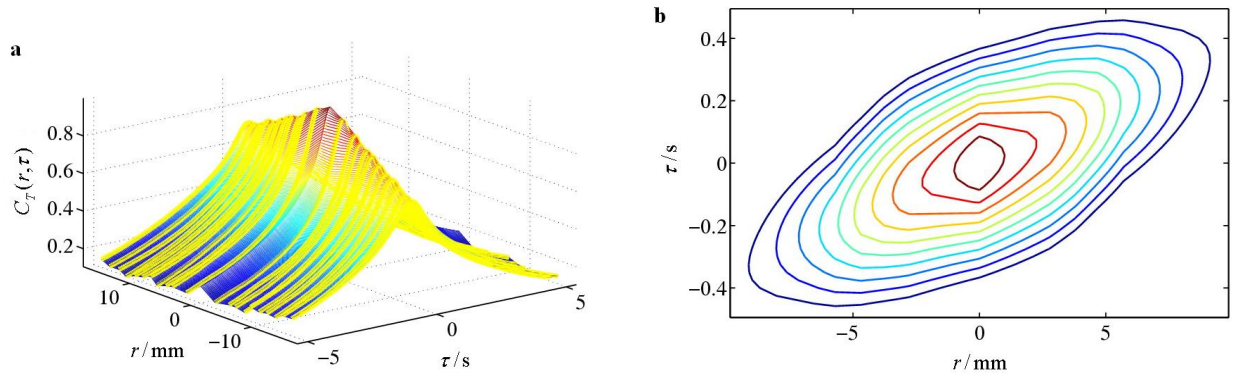

Fig. 4 **a** 3D plot of the measured space-time correlation function $C_T(r,\tau)$ as a function of r and τ; **b** 2D plot of the iso-correlation contours of the measured $C_T(r,\tau)$ in the r-τ plane with the correlation amplitude varied from 0.98 to 0.8 at decrements of 0.02 (inner to outer contours). The correlation amplitude is color coded. All the measurements are conducted near the sidewall at the mid height of the cell with $Ra = 1.4 \times 10^{10}$

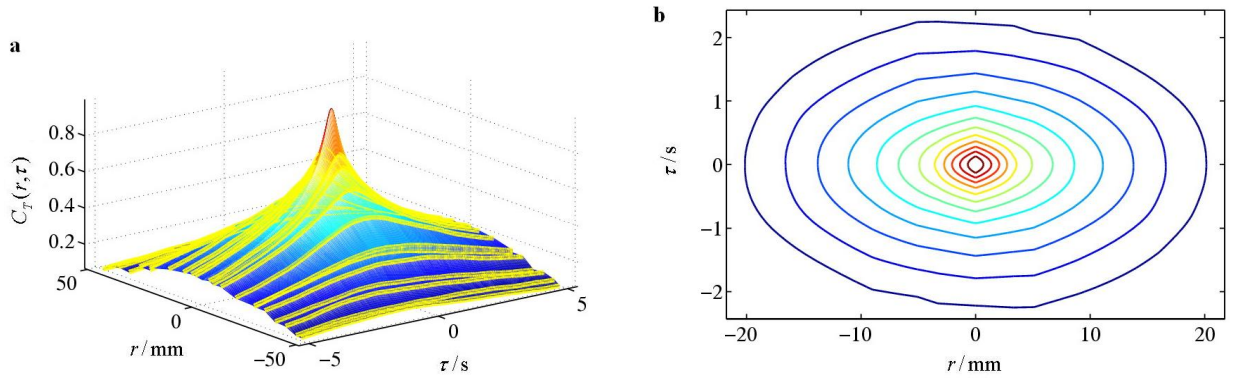

Fig. 5 **a** 3D plot of the measured space-time correlation function $C_T(r,\tau)$ as a function of r and τ; **b** 2D plot of the iso-correlation contours of the measured $C_T(r,\tau)$ in the r-τ plane with the correlation amplitude varied from 0.95 to 0.4 at decrements of 0.05 (inner to outer contours). The correlation amplitude is color coded. All the measurements are conducted at the cell center with $Ra = 1.7 \times 10^{10}$

In general, one can obtain both the values of U and V from the measured $C_T(r,\tau)$ by using Eq. (2). Figure 6 shows a comparison between the two space-time correlation functions, one is measured at a single point ($r_0 = 0$, red solid line with dots) and the other is measured at two points separated by a distance $r_0 = 3.68$ mm (black dashed line with dots). According to Eq. (2), the peak position τ_p, at which $C_T(r_0,\tau_p)$ reaches the maximum value, satisfies the equation

$$\frac{\partial r_E(r_0,\tau_p)}{\partial \tau} = 0. \tag{12}$$

Solving Eq. (12), one finds

$$\tau_p = \alpha_p r_0, \tag{13}$$

where $\alpha_p = U/(U^2 + V^2)$.

The two red stars in Fig. 1 show two special positions $(r_0, 0)$ and $(0, \tau_0)$; both of them satisfy Eq. (2) for a common value of r_E. At these two positions, the space-time correlation function $C_T(r,\tau)$ [$= C_T(r_E, 0)$] has the sample value

$$C_T(r_0, 0) = C_T(0, \tau_0). \tag{14}$$

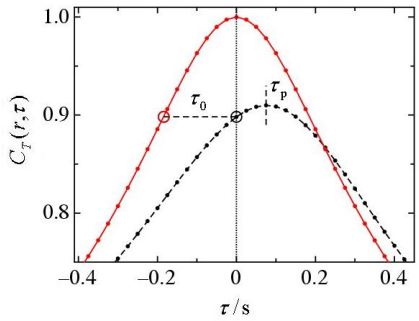

Fig. 6 Measured space-time correlation function $C_T(r_0,\tau)$ as a function of τ at a fixed value of $r_0 = 0$ (red solid line with dots) and $r_0 = 3.68$ mm (black dashed line with dots). The dots are separated by 25 ms in time, corresponding to the sampling rate of 40 Hz used in the experiment. The short vertical black dashed line indicates the position of τ_p when $C_T(r_0,\tau_p)$ reaches the maximal value. The length of the horizontal black dashed line indicates the value of τ_0, which satisfies the equation $C_T(0,\tau_0) = C_T(r_0, 0)$. All the measurements are made at the cell center with $Ra = 1.7 \times 10^{10}$

Substituting the two positions into Eq. (2), one finds

$$\tau_0 = \alpha_0 r_0, \tag{15}$$

where $\alpha_0 = 1/(U^2+V^2)^{1/2}$. Equations (13) and (15) are valid for any values of r_0 so long as the elliptic model works. By measuring the values of τ_p and τ_0 for a range of values of r_0, one can obtain the two slopes α_p and α_0 in Eqs. (13) and (15). The two characteristic velocities U and V in the elliptic model are given by

$$U = \frac{\alpha_p}{\alpha_0^2}, \tag{16}$$

and

$$V = \frac{[1-(\alpha_p/\alpha_0)^2]^{1/2}}{\alpha_0}. \tag{17}$$

Figure 7a shows the obtained values of τ_p and τ_0 as a function of r near the sidewall, where the amplitudes U and V are comparable. It is seen that in the range of $r \lesssim 13$ mm (as indicated by the vertical dotted line), the two characteristic times change linearly with r, as predicted by Eqs. (13) and (15). For $r \gtrsim 13$ mm, the data show slight deviations from the linear dependence in r, indicating that the requirements of the elliptic model are not completely satisfied beyond this range of r. We now compare this value of r with the Kolmogorov dissipation length in turbulent convection, which is estimated to be [40]

$$\eta = LPr^{1/2}/(NuRa)^{1/4}, \tag{18}$$

where Nu is the Nusselt number representing the normalized vertical heat flux. Using the measured $Nu = 0.17Ra^{0.29}$ in a similar convection cell [32], we find $\eta \simeq 0.35$ mm at $Ra = 1.4\times10^{10}$ [34]. Thus the working range r of the elliptic model is up to 37η near the sidewall.

Figure 7b shows the obtained values of τ_p and τ_0 as a function of r at the cell center, where the mean flow velocity $U_0 \simeq 0$. As predicated in Eq. (13) with $U = 0$, the measured $\tau_p \simeq 0$ for all values of r up to $r \lesssim 17$ mm (as indicated by the vertical dotted line), which corresponds to 52η for $Ra = 1.7\times10^{10}$. Within this range of r, the measured τ_0 is well described by a linear function $\tau_0 = \alpha_0 r$ with the slope $\alpha_0 = 0.116$ mm/s (dashed line). With the obtained values of α_p and α_0, one can calculate the two characteristic velocities U and V using Eqs. (16) and (17). Figure 7 thus demonstrates that the elliptic form of the iso-correlation contours, as predicted in Eq. (2), is not only valid near the origin but is also a good approximation for larger values of r and τ in the inertial range of turbulent convection.

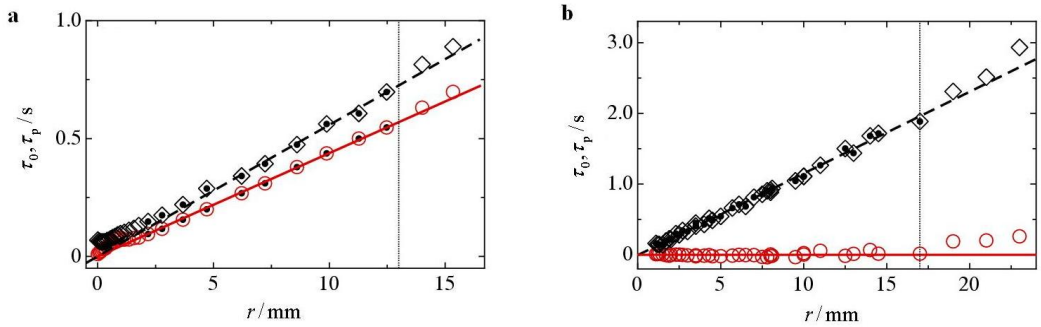

Fig. 7 (Colour online) **a** Obtained values of τ_0 (black diamonds) and τ_p (red circles) as a function of r near the sidewall with $Ra = 1.4\times10^{10}$. The data points with black dots are used for the two linear fits: $\tau_0 = \alpha_0 r$ with $\alpha_0 = 5.578\times10^{-2}$ mm/s (black dashed line) and $\tau_p = \alpha_p r$ with $\alpha_p = 4.355\times10^{-2}$ mm/s (red solid line). The vertical dotted line indicates $r = 13$ mm; **b** Obtained values of τ_0 (black diamonds) and τ_p (red circles) as a function of r at the cell center with $Ra = 1.7\times10^{10}$. The red horizontal solid line indicates $\tau_p = 0$. The black dashed line shows the linear fit, $\tau_0 = \alpha_0 r$ with $\alpha_0 = 0.116$ mm/s, to the black diamonds with dots. The vertical dotted line indicates $r = 17$ mm

To further verify the elliptic model, we plot, in Fig. 8a, the measured $C_T(r,\tau)$ as a function of the combined space-time separation r_E on a logarithmic scale. The measurements are conducted near the sidewall with different values of r and τ. The value of r_E is calculated using Eq. (2) with $U = 14.0$ mm/s and $V = 11.2$ mm/s, which are obtained from the measurements of τ_p and τ_0, as described above. It is seen that the measured $C_T(r,\tau)$'s with different values of r and τ are all collapsed onto a master curve $C_T(r_E,0)$, once the values r and τ are re-scaled as the combined space-time separation r_E given in Eq. (2). Figure 8a also reveals that the directly measured space correlation function $C_T(r,0)$ (red squares) coincides with the master curve $C_T(r_E,0)$. When $\tau = 0$, one finds $r = r_E$ from Eq. (2) and thus $C_T(r,0) = C_T(r_E,0)$. The same excellent agreement has also been found for the measured $C_T(r,\tau)$'s at the cell center [23]. The measured $C_T(r,\tau)$ curves with different values of r and τ can all be brought into coincidence with a master curve $C_T(r_E,0)$, once r_E is used as a scaling length. Figure 8a thus further confirms that the elliptic approximation given in Eqs. (2) and (7) is indeed a good approximation for the measured space-time correlation functions in turbulent convection.

An important prediction of the elliptic model is that when $r = 0$ (single-point measurement), one has $C_T(0,\tau) =$

$C_T(r_E, 0)$ with

$$r_E = (U^2 + V^2)^{1/2}\tau = V_{\text{eff}}\tau, \tag{19}$$

where V_{eff} is given by

$$V_{\text{eff}} \equiv \sqrt{U^2 + V^2} = \alpha_0^{-1}. \tag{20}$$

It should be pointed out that Eq. (19) is valid even when the Taylor frozen-flow hypothesis does not hold. For comparison, we plot, in Fig. 8b, the same measured $C_T(r, \tau)$'s as in Fig. 8a but as a function of τ for different values of r in linear scales. It is seen that the peak amplitude of the measured $C_T(r, \tau)$ decreases and its width increases with increasing r. The broadening of $C_T(r, \tau)$ is caused by the large velocity fluctuations near the sidewall, which are characterized by the rms velocity V in Eq. (20). Given these properties, the measured $C_T(r, \tau)$ near the sidewall cannot be scaled into a single master curve as shown in Fig. 8a using the linear equation $r_E = U\tau$, as predicted by the Taylor frozen-flow hypothesis. This linear equation is valid only when the rms velocity V becomes much smaller than the mean velocity U.

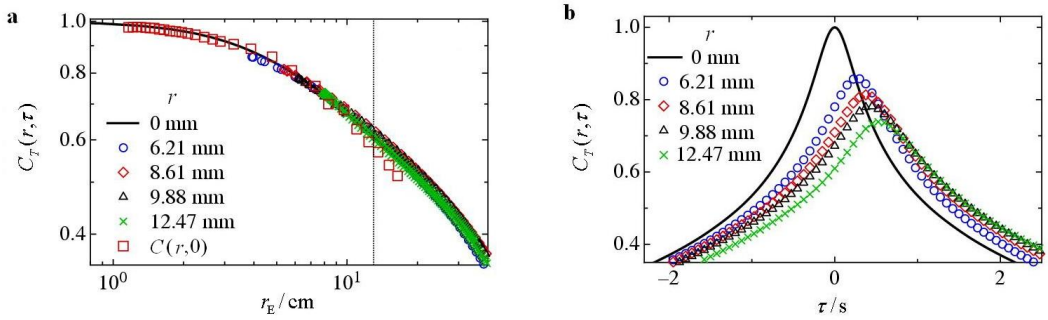

Fig. 8 **a** Measured space-time correlation function $C_T(r, \tau)$ as a function of the combined space-time separation r_E on logarithmic scales. The measurements are made near the sidewall at $Ra = 1.4 \times 10^{10}$ and with varying values of r: 0 mm (black solid line), 6.21 mm (blue circles), 8.61 mm (red diamonds), 9.88 mm (black triangles), 12.47 mm (green crosses). The red squares are the directly measured space correlation function $C_T(r, 0)$ as a function of r (= r_E). The values of r_E are calculated using Eq. (2) with $U = 14.0$ mm/s and $V = 11.2$ mm/s. The vertical dotted line indicates $r_E = 13$ mm; **b** Same correlation functions as in **a** plotted as a function of τ for different values of r in linear scales

3.3 Velocity space-time correlations

The elliptic model is also tested recently for the velocity space-time correlation function $C_u(r, \tau)$ in turbulent RBC [24]. The velocity measurements were carried out using PIV in a vertical cylindrical cell with the aspect-ratio $\Gamma = 1$ (both the cell diameter D and height L equal to 50 cm) at fixed values of $Ra = 9.5 \times 10^{10}$ and $Pr = 5.5$. The velocity field was measured in the rotation plane of the LSC. It was found that the iso-correlation contours of the measured $C_u(r, \tau)$ for the vertical velocity near the sidewall have a similar elliptic shape as those shown in Fig. 4b with an orientation angle determined by the values of U and V. At the cell center where $U \simeq 0$, the iso-correlation contours of the measured $C_u(r, \tau)$ for both the vertical and horizontal velocity are similar to those shown in Fig. 5b with their two major axes coincided with the r and τ axes, respectively. The experiment, therefore, verified the predictions of the elliptic model as shown in Eqs. (2) and (7) for the velocity field. The values of U and V deduced from the measured $C_u(r, \tau)$ were compared with those directly measured by PIV. The obtained value of U was found to be very close to the directly measured mean velocity U_0. The values of V obtained in the measuring plane, however, were found to be systematically larger than the measured rms velocity σ_u by a factor of 1.87 for the vertical velocity measurements and by a factor of 4.21 for the horizontal velocity measurements.

The velocity space-time correlation function $C_u(r, \tau)$ was also measured in a random swirling flow [41]. The swirling flow was generated between two horizontal disks with the top disk driven by a commercial rheometer, which shears the fluid between the two disks at a constant rotation rate. The aspect-ratio of the flow cell was $\Gamma = 4.8$ and the velocity measurements were carried out using PIV in the midplane between the two horizontal disks. Being sheared by the rotating disk, the flow structure was found to be close to that of a fly wheel with the mean velocity $U_0 \simeq 0$ at the center, increasing radially away from the center, and reached a maximum value near the sidewall. This flow structure is quite similar to that in the plane of the LSC in turbulent convection, where Taylor's frozen-flow hypothesis does not hold. It was found that [41] the iso-correlation contours of the measured $C_u(r, \tau)$ have an elliptic shape as predicted by the elliptic model. The measured values of τ_0 and τ_p were found to increase linearly with r, as shown in Eqs. (13) and (15), but the obtained slopes α_0 and α_p were found to disagree with the predictions of the Taylor frozen-flow hypothesis. While the authors in Ref. [41] did not use the elliptic model to interpret their data, it is clearly seen from Eqs. (13) to (17) that the deviations from the Taylor hypothesis can be well explained by including the contributions of both U and V, as shown in Eq. (2).

4 Applications of space-time correlation functions

The successful test of the elliptic model allows us to have a reliable analytic relationship between space and time in the velocity correlation function $C_u(r,\tau)$ and temperature correlation function $C_T(r,\tau)$, which has a wide variety of applications in the analysis of experimental and numerical data obtained at either a single point or multiple points and in the study of the statistical properties of small-scale turbulence. In this section, we discuss a few examples.

4.1 Finding velocity information from two-point temperature measurements

In some convective flows, such as turbulent RBC in low temperature helium gas [16, 17, 42], direct measurement of the local velocity field is very difficult. In this case, one can obtain the mean velocity U and rms velocity V from multipoint temperature measurements. As shown in Fig. 7, when the values of τ_p and τ_0 are measured at a number of separations r, one can obtain the slopes α_p and α_0 from the two linear plots and calculate the two characteristic velocities U and V, respectively, using Eqs. (16) and (17). This method was first applied in a high-pressure thermal convection experiment [43] with two-point temperature measurements separated by a distance r_0. The measurements used two separation values, 0 and r_0. Later, it was used for three-point temperature measurements with uneven separations, resulting in four values of separation r. This method has been proven to be a useful technique to obtain the velocity information and can be used in many practical flows in opaque fluids and in low-temperature, high-pressure, or low-vacuum gases, where one can conduct temperature measurements but it is difficult to conduct direct velocity measurement.

4.2 Finding velocity information from shadowgraph image measurements

As mentioned above, in turbulent Rayleigh–Bénard convection, temperature as a passive scalar follows the local flow everywhere in the bulk region of the convection cell except near the upper and lower thermal boundary layers. In addition to being a directly measurable passive scalar, temperature fluctuations in turbulent convection also produce a fluctuating refractive index field in the convecting fluid. Such a fluctuating field can be visualized using the shadowgraph technique, which measures a longitudinal average (along the light path) of the lateral Laplacian of the refractive index field [44]. The shadowgraph technique has been widely used in the study of pattern formation and chaos [45].

In a recent experiment, Hogg and Ahlers [25] showed that the space-time correlation function of the shadowgraph images also has the elliptic form and used the elliptic approximation to study the scaling behavior of the mean velocity U of the large-scale circulation and its rms value V in a large-aspect-ratio convection cell filled with low-Prandtl-number gas mixtures at high pressures. In the experiment, the shadowgraph-intensity correlation function $C_I(r,\tau)$ is defined as

$$C_I(r,\tau) = \frac{\langle \delta I(x+r,t+\tau)\delta I(x,t)\rangle_{t,x}}{\sigma_I(x+r)\sigma_I(x)}, \tag{21}$$

where $\langle\cdots\rangle_{t,x}$ denotes a space and time average, $\delta I(x,t) = I(x,t) - \langle I\rangle$ is the intensity variation of the shadowgraph image, and $\sigma_I(x+r)$ and $\sigma_I(x)$ are, respectively, the rms values of δI at positions $x+r$ and x. In Eq. (21), the spatial separation r is obtained for each pair of pixels in the same image. The value of τ is given by the time difference between the i-th and j-th images in the sequence. Compared to the local temperature and/or velocity measurements at fixed locations, the measured $C_I(r,\tau)$ from the shadowgraph images is averaged over the viewing area. Thus the obtained values of U and V are averaged quantities over the viewing area as well as over the measuring time. This method of obtaining velocity information can also be extended to other flow visualization images.

4.3 Finding wave-number spectrum from single-point frequency power spectrum

For many practical flows of interest, experimental information about small-scale turbulent fluctuations is often limited to the time series measurement of the local temperature (or velocity) at a single or a few spatial positions, from which one obtains the temporal correlation function $C_T(0,\tau)$ or its Fourier transform $E_T(f)$. The interpretation of the measured $E_T(f)$ is often made using the Taylor frozen-flow hypothesis without a further justification about whether it is valid for a particular flow of concern [20, 46].

As discussed in Sect. B, the temperature space correlation function and temporal correlation function are connected via the equation

$$C_T(r,0) = C_T(0,\tau), \tag{22}$$

where $r = V_{\rm eff}\tau$. For small values of r and τ, both sides of Eq. (22) can be expanded up to the second order

$$\begin{aligned} C_T(r,0) &= 1 - \frac{1}{2}\frac{r}{\lambda_0} + \cdots, \\ C_T(0,\tau) &= 1 - \frac{1}{2}\frac{\tau}{\lambda_\tau} + \cdots, \end{aligned} \tag{23}$$

where λ_τ is a micro-scale decay time analogous to the Taylor micro-scale λ_0. Substituting Eq. (23) into Eq. (22), one immediately finds $\lambda_0 = V_{\rm eff}\lambda_\tau$. Taking the Fourier transform of both equations in Eq. (23), one finds [22]

$$E_T(k\lambda_0) = E_T(f\lambda_\tau). \tag{24}$$

Equation (24) states that the power spectrum $E_T(f\lambda_\tau)$ in the frequency domain is equivalent to the power spectrum $E_T(k\lambda_0)$ in the k-space, once the wave number k is scaled by λ_0 and the frequency f is scaled by λ_τ. Equation (24) thus can be used to obtain the wave-number power spectrum $E_T(k\lambda_0)$ from the single-point time series measurements, even when the Taylor frozen-flow hypothesis does not hold [47].

5 Concluding remarks

The space-time correlation functions $C_u(r,\tau)$ for a velocity field and $C_T(r,\tau)$ for a passive scalar field, such as temperature fluctuations in the bulk region of turbulent RBC, are important functions that are used to describe the statistical properties of small-scale turbulence. Theoretical predictions are given in space and experimental information about small-scale turbulent fluctuations is often limited to the time series measurement at a single or a few spatial locations. Finding a connection between the time-domain results and the theoretical predictions made in the real space (or in the Fourier space) beyond Taylor's frozen-flow hypothesis is therefore of fundamental interest and of practical importance to the study of fluid turbulence.

The recently developed elliptic model showed that for a stationary and homogenous turbulent flow with two characteristic velocities, the mean velocity U and a fluctuating velocity V, its space-time correlation function $C_u(r,\tau)$ [or $C_T(r,\tau)$] has a scaling form $C_u(r_E,0)$ [or $C_T(r_E,0)$], where the combined space-time separation r_E is given in Eq. (2). This elliptic relationship between r and τ is exact up to second order and may also hold for large values of r and τ if the flow is scale-invariant. A number of experiments have been carried out recently to study the scaling behavior of the space-time correlation functions in turbulent RBC. These experiments verified the elliptic model and demonstrated its applications to a class of turbulent flows in which the requirement of Taylor's frozen-flow hypothesis is not met. In addition to the space-time correlation functions, there are other space-time functions used to describe the statistical properties of small-scale turbulence. Examples include higher-order space-time correlation functions, space-time structure functions, and space-time joint probability density functions. How the space and time are connected in these functions need to be addressed in future theoretical and experimental investigations.

Acknowledgement The project was supported in part by RGC of Hong Kong SAR (HKUST-605013). We have benefited from many useful discussions with He, G.-W.. He, X. is very grateful to Ahlers, G. for illuminating discussions about the elliptic model application in shadowgraph image measurements.

References

1 Mellor, G.L., Yamada, T.: Development of a turbulence closure model for geophysical fluid problems. Reviews of Geophysics and Space Physics, **20**, 851–875 (1982)
2 Sreenivasan, K.R.: Fluid turbulence. Rev. Mod. Phys. **71**, 383–395 (1999)
3 Wallace, J.M.: Space-time correlations in turbulent flow: A review. Theor. Appl. Mech. Lett. **4**, 022003 (2014)
4 Kolmogorov, A.N.: The local structure of turbulence in incompressible viscous fluid for very large Reynolds numbers. Dokl. Akad. Nauk SSSR, **30**, 9 (1941)
5 Townsend, A.A.: The Structure of Turbulence Shear Flow. Cambridge University Press, Cambridge, England (1976)
6 Warhaft, Z.: Passive scalars in turbulent flows. Annu. Rev. Fluid Mech. **32**, 203–240 (2000)
7 Smits, A.J., McKeon, B.J., Marusic, I.: High Reynolds number wall turbulence. Annu. Rev. Fluid Mech. **43**, 353–375 (2011)
8 Taylor, G.I.: The spectrum of turbulence. Proc. R. Soc. London A, **164**, 476 (1938)
9 Sreenivasan, K.R., Antonia, R.A.: The phenomenology of small-scale turbulence. Annu. Rev. Fluid Mech. **29**, 435–472 (1997)
10 Pope, S.B.: Turbulent Flow. Cambridge University Press, Cambridge, England (2000)
11 Kraichnan, R.: Kolmogorov's hypotheses and Eulerian turbulence theory. Phys. Fluids, **7**, 1723 (1964)
12 Tennekes, H.: Eulerian and Lagrangian time microscales in isotropic turbulence. J. Fluid Mech. **67**, 561–567 (1975)
13 Frisch, U.: Turbulence: The Legacy of A. N. Kolmogorov. Cambridge University Press, Cambridge, UK (1995)
14 Tennekes, H., Lumley, J.L.: A First Course in Turbulence. The MIT Press, Cambridge, Massachusetts (1972)
15 Pinton, J.F., Labbé, R.: Correction to the Taylor hypothesis in swirling flows. J. Phys. II France, **4**, 1461–1468 (1994)
16 Sano, M., Wu, X.Z., Libchaber, A.: Turbulence in helium-gas free convection. Phys. Rev. A, **40**, 6421–6430 (1989)
17 Niemela, J.J., Skrbek, L, Sreenivasan, K.R., et al.: The wind in confined thermal convection. J. Fluid Mech. **449**, 169–178 (2001)
18 Sun, C., Zhou, Q., Xia, K.Q.: Cascades of velocity and temperature fluctuations in buoyancy-driven thermal turbulence. Phys. Rev. Lett. **97**, 144504 (4 pages) (2006)
19 Lohse, D., Xia, K.Q.: Small-scale properties of turbulent Rayleigh-Bénard convection. Annu. Rev. Fluid Mech. **42**, 335–364 (2010)
20 He, G.W., Zhang, J.B.: Elliptic model for space-time correlations in turbulent shear flows. Phys. Rev. E, **73**, 055303 (4 pages) (2006)
21 Zhao, X., He, G.W.: Space-time correlations of fluctuating velocities in turbulent shear flows. Phys. Rev. E, **79**, 046316 (12 pages) (2009)
22 He, X., He, G.W., Tong, P.: Small-scale turbulent fluctuations beyond Taylor's frozen-flow hypothesis. Phys. Rev. E, **81**, 065303 (4 pages) (2010)
23 He, X., Tong, P.: Kraichnans random sweeping hypothesis in homogeneous turbulent convection. Phys. Rev. E, **83**, 037302 (4 pages) (2011)
24 Zhou, Q., Li, C.M., Lu, Z.M., et al.: Experimental investigation of longitudinal space-time correlations of the velocity field in turbulent Rayleigh–Bénard convection. J. Fluid Mech. **683**, 94–111 (2011)
25 Hogg, J., Ahlers, G.: Reynolds-number measurements for low-Prandtl-number turbulent convection of large-aspect-ratio samples. J. Fluid Mech. **725**, 664–680 (2013)
26 He, G.W., Jin, G.D., Zhao, X.: Scale-similarity model for lagrangian velocity correlations in isotropic and stationary turbulence. Phys. Rev. E, **80**, 066313 (7 pages) (2009)
27 Wilczek, M., Narita, Y.: Wave-number frequency spectrum for turbulence from a random sweeping hypothesis with mean flow. Phys. Rev. E, **86**, 066308 (8 pages) (2012)
28 Ahlers, G., Grossmann, S., Lohse, D.: Heat transfer and large scale dynamics in turbulent Rayleigh-Bénard convection. Rev.

Mod. Phys. **81**, 503–538 (2009)
29 Ahlers, G.: Turbulent convection. Physics, **2**, 74 (7 pages) (2009)
30 Chillá, F., Schumacher, J.: New perspectives in turbulent Rayleigh–Bénard convection. Eur. Phys. J. E, **35**, 58 (2012)
31 Lui, S.L., Xia, K.Q.: Spatial structure of the thermal boundary layer in turbulent convection. Phys. Rev. E, **57**, 5494–5503 (1998)
32 Du, Y.B., Tong, P.: Turbulent thermal convection in a cell with ordered rough boundaries. J. Fluid Mech. **407**, 57 (2000)
33 Ahlers, G., Bodenschatz, E., Funfschilling, D., et al.: Logarithmic temperature profiles in turbulent Rayleigh–Bénard convection. Phys. Rev. Lett. **109**, 114501 (5 pages) (2012)
34 He, X., Ching, E.S.C., Tong, P.: Locally averaged thermal dissipation rate in turbulent thermal convection: A decomposition into contributions from different temperature gradient components. Phys. of Fluids, **23**, 025106 (13 pages) (2011)
35 He, X., Tong, P., Ching, E.S.C.: Statistics of the locally averaged thermal dissipation rate in turbulent Rayleigh–Bénard convection. J. of Turbul. **11**, 1–10 (2010)
36 Ching, E.S.C., Tsang, Y.K., Fok, T.N., et al.: Scaling behavior in turbulent Rayleigh–Bénard convection revealed by conditional structure functions. Phys. Rev. E, **87**, 013005 (6 pages) (2013)
37 Qiu, X.L., Tong, P.: Large scale velocity structures in turbulent thermal convection. Phys. Rev. E, **64**, 036304 (13 pages) (2001)
38 Zhou, Q., Sun, C., Xia, K.Q.: Experimental investigation of homogeneity, isotropy, and circulation of the velocity field in buoyancy-driven turbulence. J. Fluid Mech. **598**, 361–372 (2008)
39 He, X., Tong, P.: Measurements of the thermal dissipation field in turbulent Rayleigh–Bénard convection. Phys. Rev. E, **79**, 026303 (14 pages) (2009)
40 Cioni, S., Ciliberto, S., Sommeria, J.: Temperature structure functions in turbulent convection at low Prandtl number. Europhys. Lett. **32**, 413–418 (1995)
41 Burghelea, T., Segre, E., Steinberg, V.: Validity of the Taylor hypothesis in a random spatially smooth flow. Physics of Fluids, **17**, 103101 (8 pages) (2005)
42 Castaing, B., Gunaratne, G., Heslot, F., et al.: Scaling of hard thermal turbulence in Rayleigh–Bénard convection. J. Fluid Mech. **204**, 1–30 (1989)
43 He, X., Funfschilling, D., Nobach, H., et al.: Transition to the ultimate state of turbulent Rayleigh–Bénard convection. Phys. Rev. Lett. **108**, 024502 (5 pages) (2012)
44 de Bruyn, J.R., Bodenschatz, E., Morris, S.W., et al.: Apparatus for the study of Rayleigh–Bénard convection in gases under pressure. Rev. Sci. Instrum. **67**, 2043 (1996)
45 Bodenschatz, E., Pesch, W., Ahlers, G.: Recent developments in Rayleigh–Bénard convection. Annu. Rev. Fluid Mech. **32**, 709–778 (2000)
46 Bouruet-Aubertot, P., Van Haren, H., Lelong, M.P.: Stratified inertial subrange inferred from in situ measurements in the bottom boundary layer of the rockall channel. J. Phys. Oceanogr. **40**, 2401 (2010)
47 He, X., van Gils, D.P.M., Bodenschatz, E., et al.: Logarithmic spatial variations and universal f^{-1} power spectra of temperature fluctuations in turbulent Rayleigh–Bénard convection. Phys. Rev. Lett. **112**, 174501 (5 pages) (2014)